Evolving viscous anisotropy in the upper mantle and its geodynamic implications

Á. Király[1], C.P. Conrad[1], L.N. Hansen[2]

[1] Centre for Earth Evolution and Dynamics, University of Oslo, Norway

[2] Department of Earth and Environmental Sciences, University of Minnesota, Minneapolis, MN, USA

Key Points

- Olivine texture develops with asthenospheric deformation, yielding directional variations in viscosity of more than an order of magnitude
- Shearing of textured olivine is easy parallel to the dominant a- and b-axis orientations but difficult parallel to the dominant c-axis
- Anisotropic viscosity promotes faster plate motions, subduction initiation and dripping, but impedes directional changes in plate motions

Key words

Olivine, Anisotropic viscosity, LPO, Texture development, Plate motions, Asthenospheric deformation

Abstract

Asthenospheric shear causes some minerals, particularly olivine, to develop anisotropic textures that can be detected seismically. In laboratory experiments, these textures are also associated with anisotropic viscous behavior, which should also be important for geodynamic processes. To examine the role of anisotropic viscosity for asthenospheric deformation, we developed a numerical model of coupled anisotropic texture development and anisotropic viscosity, both calibrated according to laboratory measurements of olivine aggregates. This model characterizes the time-dependent coupling between large-scale formation of LPO textures and changes in asthenospheric viscosity for a series of deformation paths that are representative of upper-mantle geodynamic processes. We find that texture development beneath a moving surface plate tends to align the a-axes of olivine into the plate motion direction, which weakens the effective viscosity in this direction and increases plate velocity for a given driving force. We demonstrate that the effective viscosity increases for shear in the horizontal direction perpendicular to the a-axes. This increase should slow plate motions and new texture development in this perpendicular direction, and can impede changes to the plate motion direction for 10s of Myrs. However, the same well-developed asthenospheric texture should foster both subduction initiation and lithospheric gravitational instabilities as vertical deformation is favored across a sub-lithospheric olivine texture, and the sheared texture can quickly rotate into a vertical orientation. These end-member cases examining shear-deformation in the presence of a well formed asthenospheric texture illustrate the importance of the mean olivine orientation, and its associated viscous anisotropy, for a variety of geodynamic processes.

Plain language summary

The uppermost layer of Earth's mantle, the asthenosphere, experiences large deformations due to a variety of tectonic processes. During deformation, grains of olivine, the main rock-forming mineral in the asthenosphere, rotate into a preferred direction parallel to the deformation developing a texture that can affect the asthenosphere response to tectonic stresses. Laboratory measurements show that the deformation rate depends on the orientation of the shear stress relative to the olivine texture. Here, we use numerical models to apply the findings of the laboratory measurements to geodynamic situations that are difficult to simulate in a laboratory. These models track the development of olivine texture and its directional response to shear stress, which are highly coupled. Our results suggest that anisotropic viscosity in the asthenosphere can significantly affect the motions of tectonic plates, as plate motion in a continuous direction should become faster while abrupt changes in the direction of plate motion should meet high resistance in the underlying asthenosphere. We suggest that olivine textures in the asthenosphere play a critical role in upper mantle dynamics.

1. Introduction

The physical parameters of the upper mantle, such as its density and rheology, control a variety of surface features, such as general tectonic regime, faulting characteristics, dynamic topography, and plate velocity. Many of these features are thus related to the properties of olivine, which comprises ~60% of the upper mantle (Stixrude and Lithgow-Bertelloni, 2005). It has long been known that olivine is anisotropic in its elastic properties, and this directional dependence has been observed in the upper mantle using seismic waves (e.g., Tanimoto and Anderson, 1984). This observed seismic anisotropy is mainly the result of the lattice preferred orientation (LPO, or texture) of the olivine crystals, which causes the speed of seismic waves to depend on propagation direction and additionally causes shear waves to split into two perpendicularly polarized waves (faster and slower) (Bamford and Crampin, 1977; Christensen, 1984; Mainprice et al., 2015). The texture (or LPO) itself is thought to result from shear strain in the upper mantle, which causes olivine crystals to rotate into a preferred direction, generally with the seismically fast axis parallel to the direction of shearing (e.g., Ribe, 1989; Karato and Wu, 1993). Seismic observations of this anisotropy have been used to infer patterns of upper-mantle deformation (Long and Becker, 2010), for example related to tectonic plate motions (e.g., Becker, 2008; Becker et al., 2014, 2008, 2003; Behn et al., 2004; Conrad and Behn, 2010; Gaboret et al., 2003), subduction (e.g., Long, 2013), continental collision (e.g., Silver, 1996), and motion on transform faults (e.g., Eakin et al., 2018).

Early laboratory experiments found that olivine is not limited to anisotropy in its elastic properties, but also exhibits anisotropy in its viscosity. Durham and Goetze (1977) demonstrated that the deformation rate of a single olivine crystal is orientation dependent and can vary by a factor of 50. To assess the role of single-crystal anisotropy in controlling the anisotropy of an aggregate of crystals, Hansen et al. (2012) first deformed aggregates of olivine in torsion and subsequently deformed them in extension. In torsion, the samples gradually weaken as the LPO forms, but subsequent extensional deformation normal to the initial shear plane is characterized by a factor of 14 increase in viscosity. Similarly, but in a reverse order, Hansen et al., (2016b) first deformed aggregates of olivine in extension and subsequently deformed them in torsion. In extension, the samples gradually weaken as the LPO forms, but subsequent torsional deformation is again characterized by much higher viscosities. Taken together, these experiments demonstrate that prolonged deformation in a consistent orientation leads to texture formation that reduces the viscosity, and a subsequent change in the orientation of deformation results in a dramatic increase in the viscosity.

However, Hansen et al.’s (2016b) laboratory experiments were only able to test a small number of deformation paths (i.e., first extension then torsion and vice versa), making it difficult to directly apply their results to deformation in the mantle. To apply their results more generally to mantle deformation, Hansen et al., (2016a) used the existing experiments to define and calibrate a mechanical model of slip-system activities and texture development within olivine aggregates. This model can predict both the evolution of olivine textures and the associated anisotropic viscous behavior for olivine aggregates undergoing arbitrary deformation paths. This coupled micromechanical and textural development model enables us to investigate the role of viscous anisotropy for a range of geodynamic processes.

Decades ago, researchers used early numerical modeling techniques to test the relevance of viscous anisotropy on geodynamical processes, such as mantle convection or post-glacial rebound (Christensen, 1987). These studies relied on the laboratory measurements of Durham and Goetze (1977), which constrained the anisotropic behavior of single olivine crystals, and the work of Karato (1987), who studied the mechanisms of olivine texture formation. Due to the absence of more detailed laboratory data, previous modelers assumed transverse isotropy in a two-dimensional mantle (i.e., isotropic viscosity for shearing in the horizontal plane, and anisotropy expressed as differences between shearing in the horizontal and vertical directions). More recently, the effect of anisotropic viscosity on mantle convection has been revisited (Mühlhaus et al., 2003), with additional investigations into Raleigh-Taylor instabilities and subduction-zone processes within an anisotropically viscous mantle and/or lithosphere (Lev and Hager, 2011, 2008). These studies are based on the director method (Mühlhaus et al., 2002), which models olivine orientations as a set of directors, that is, 2D unit vectors pointing normal to the easy glide plane. Anisotropic viscosity is expressed by a combination of normal and shear viscosities, and the effective shear viscosity is a function of the distribution of the directors. Furthermore, because the directors are advected and rotated by the flow, this method couples texture development to the anisotropic viscosity of the mantle. The 2D nature of the director method, however, limits its ability to capture the complete anisotropy associated with olivine, which has three independent slip systems that accommodate deformation at different rates (Hansen et al., 2016a).

Here we have modified the director method to accommodate three-dimensional deformations of olivine aggregates using the micromechanical approach of Hansen et al. (2016a). This model is calibrated by laboratory constraints on slip system activities and parameters of texture development (i.e., the relative rotation rates of the different olivine slip systems). The resulting model allows us to explore both the texture development of an olivine aggregate in a wide range of deformation paths and the mechanical response of these textured aggregates to applied stresses associated with these deformation paths. Our goal is to create first-order models of tectonic plate movement subject to a continuous driving force (e.g., slab pull) in one direction. As the olivine texture develops in the asthenosphere, we expect the mechanical response of the system to change as a function of time and accumulated strain, resulting in a changing plate velocity. Next, by changing the direction of the driving force, we can examine the response of the system to the application of stress in a new direction. The resulting deformation paths are analogs for geodynamic applications such as changes in the direction of plate movement, lithospheric dripping, initiation of subduction, and transform faulting. These simple exercises lead us to a better understanding of the interplay among olivine-texture development, anisotropic mantle rheology, and large-scale geodynamic processes.

2. Methods

2.1 Mathematical formulation

Our method is based on the micromechanical model described and characterized by Hansen et al. (2016a). This approach uses a pseudo-Taylor approximation (after Taylor, 1938) to calculate the stress needed to create an equivalent strain rate on each olivine crystal, allowing for slip along three linearly independent slip systems. The micromechanical model is coupled to a texture development model, in which the deformation of the olivine aggregate results in grain rotations. The rotation rate depends on the orientation of each grain with respect to the deformation, and a set of texture parameters that define the relative rotation rates along the four olivine slip systems. These combined models provide the basis for a method to calculate the anisotropic viscosity (or conversely, the fluidity) for any given olivine texture. The resulting three-dimensional tensor can then be used to predict the deformation behavior for several geodynamic applications. In the following, we present details of this method and the results of first-order models in which the olivine mantle undergoes different deformation paths induced by temporal variations in an applied shear stress.

To calculate the strain rate induced by the imposed stress, some further steps are necessary beyond those described by the mechanical model of Hansen et al. (2016a). The macroscopic constitutive relationship between stress and strain rate for an anisotropic viscous medium is

$$\sigma_{kl} = \eta_{ijkl}\dot{\varepsilon}_{ij} , \quad (1)$$

where $\dot{\varepsilon}_{ij}$ is the strain-rate tensor, σ_{kl} is the deviatoric-stress tensor, and η_{ijkl} is the viscosity tensor (Christensen, 1987; Pouilloux et al., 2007). Due to their symmetry, the deviatoric-stress and the strain-rate tensors can both be reduced to vectors using Kelvin notation, which preserves the norm of each of the tensors in (1) (Dellinger et al., 1998),

$$\dot{\varepsilon}_{ij} = \begin{bmatrix} \dot{\varepsilon}_{11} & \dot{\varepsilon}_{12} & \dot{\varepsilon}_{13} \\ \dot{\varepsilon}_{12} & \dot{\varepsilon}_{22} & \dot{\varepsilon}_{23} \\ \dot{\varepsilon}_{13} & \dot{\varepsilon}_{23} & \dot{\varepsilon}_{33} \end{bmatrix} \equiv \begin{bmatrix} \dot{\varepsilon}_{11} \\ \dot{\varepsilon}_{22} \\ \dot{\varepsilon}_{33} \\ \sqrt{2}\dot{\varepsilon}_{23} \\ \sqrt{2}\dot{\varepsilon}_{13} \\ \sqrt{2}\dot{\varepsilon}_{12} \end{bmatrix} \equiv \begin{bmatrix} \dot{\varepsilon}_{1} \\ \dot{\varepsilon}_{2} \\ \dot{\varepsilon}_{3} \\ \dot{\varepsilon}_{4} \\ \dot{\varepsilon}_{5} \\ \dot{\varepsilon}_{6} \end{bmatrix} \tag{2}$$

$$\sigma_{ij} = \begin{bmatrix} \sigma_{11} & \sigma_{12} & \sigma_{13} \\ \sigma_{12} & \sigma_{22} & \sigma_{23} \\ \sigma_{13} & \sigma_{23} & \sigma_{33} \end{bmatrix} \equiv \begin{bmatrix} \sigma_{11} \\ \sigma_{22} \\ \sigma_{33} \\ \sqrt{2}\sigma_{23} \\ \sqrt{2}\sigma_{13} \\ \sqrt{2}\sigma_{12} \end{bmatrix} \equiv \begin{bmatrix} \sigma_{1} \\ \sigma_{2} \\ \sigma_{3} \\ \sigma_{4} \\ \sigma_{5} \\ \sigma_{6} \end{bmatrix}. \tag{3}$$

It follows that the viscosity can be reduced to a 6x6 tensor (e.g., Pouilloux et al., 2007). Because of the non-linear rheological behavior of olivine, the viscosity tensor is also a function of stress. The rheology can thus be expressed by a stress-independent material constant ($\underline{\underline{A}}$), which relates to the viscosity as

$$inv(\eta_{ij}) = A_{ij} \cdot II_{\sigma}{}^{(n-1)/2}\ . \tag{4}$$

Equation 4 describes the fluidity of the material at a given stress, where II_{σ} denotes the second invariant of the deviatoric stress and *n* is the power-law factor. Using eq. (4), the strain rate can be expressed as a function of the stress and the fluidity according to

$$\begin{bmatrix} \dot{\varepsilon}_{1} \\ \dot{\varepsilon}_{2} \\ \dot{\varepsilon}_{3} \\ \dot{\varepsilon}_{4} \\ \dot{\varepsilon}_{5} \\ \dot{\varepsilon}_{6} \end{bmatrix} = \begin{bmatrix} A_{11} & A_{12} & A_{13} & A_{14} & A_{15} & A_{16} \\ A_{21} & A_{22} & A_{23} & A_{24} & A_{25} & A_{26} \\ A_{31} & A_{32} & A_{33} & A_{34} & A_{35} & A_{36} \\ A_{41} & A_{42} & A_{43} & A_{44} & A_{45} & A_{46} \\ A_{51} & A_{52} & A_{53} & A_{54} & A_{55} & A_{56} \\ A_{61} & A_{62} & A_{63} & A_{64} & A_{65} & A_{66} \end{bmatrix} \cdot \begin{bmatrix} \sigma_{1} \\ \sigma_{2} \\ \sigma_{3} \\ \sigma_{4} \\ \sigma_{5} \\ \sigma_{6} \end{bmatrix} \cdot II_{\sigma}{}^{(n-1)/2}. \tag{5}$$

To solve eq. (5) for the strain rate, the material constant $\underline{\underline{A}}$, which we will refer to as the fluidity parameter tensor, must be known. $\underline{\underline{A}}$ is a function of temperature and grain size, but also depends on the crystal orientations of the aggregate. The micromechanical model of Hansen et al. (2016a) allows us to find the stress needed to produce any strain rate for a given olivine texture. Therefore, to find the components of $\underline{\underline{A}}$ with the pseudo-Taylor mechanical model, we need to apply 6 different strain rates to the aggregate and calculate the 6 stress vectors that are required to produce these strain rates. The six strain rates define the columns of the tensor $\underline{\underline{E}}$,

$$E = \begin{bmatrix} \dot{\varepsilon}_0 & -\dot{\varepsilon}_0/2 & -\dot{\varepsilon}_0/2 & 0 & 0 & 0 \\ -\dot{\varepsilon}_0/2 & \dot{\varepsilon}_0 & -\dot{\varepsilon}_0/2 & 0 & 0 & 0 \\ -\dot{\varepsilon}_0/2 & -\dot{\varepsilon}_0/2 & \dot{\varepsilon}_0 & 0 & 0 & 0 \\ 0 & 0 & 0 & \dot{\varepsilon}_0/\sqrt{2} & 0 & 0 \\ 0 & 0 & 0 & 0 & \dot{\varepsilon}_0/\sqrt{2} & 0 \\ 0 & 0 & 0 & 0 & 0 & \dot{\varepsilon}_0/\sqrt{2} \end{bmatrix}, \qquad (6)$$

where $\dot{\varepsilon}_0$ is the applied strain rate amplitude. By applying the micromechanical model of Hansen et al. (2016a) separately to each column of $\underline{\underline{E}}$, we can compute the set of stress tensors associated with each of these six strain rates. We use these stress tensors to construct the tensor $\underline{\underline{S}}$, for which each row represents the stress vector associated with the strain-rate vector in each column of $\underline{\underline{E}}$, multiplied by $II_\sigma{}^{(n-1)/2}$. These two tensors are related according to the equation

$$\underline{\underline{E}}=\underline{\underline{A}}*\underline{\underline{S}}, \qquad (7)$$

where $\underline{\underline{S}}$=

$$\begin{bmatrix} II_{\sigma\_1}{}^{(n-1)/2}\sigma_{1\_1} & II_{\sigma\_1}{}^{(n-1)/2}\sigma_{2\_1} & II_{\sigma\_1}{}^{(n-1)/2}\sigma_{3\_1} & II_{\sigma\_1}{}^{(n-1)/2}\sigma_{4\_1} & II_{\sigma\_1}{}^{(n-1)/2}\sigma_{5\_1} & II_{\sigma\_1}{}^{(n-1)/2}\sigma_{6\_1} \\ II_{\sigma\_2}{}^{(n-1)/2}\sigma_{1\_2} & II_{\sigma\_2}{}^{(n-1)/2}\sigma_{2\_2} & II_{\sigma\_2}{}^{(n-1)/2}\sigma_{3\_2} & II_{\sigma\_2}{}^{(n-1)/2}\sigma_{4\_3} & II_{\sigma\_2}{}^{(n-1)/2}\sigma_{5\_2} & II_{\sigma\_2}{}^{(n-1)/2}\sigma_{2\_2} \\ II_{\sigma\_3}{}^{(n-1)/2}\sigma_{1\_3} & II_{\sigma\_3}{}^{(n-1)/2}\sigma_{2\_3} & II_{\sigma\_3}{}^{(n-1)/2}\sigma_{3\_3} & II_{\sigma\_3}{}^{(n-1)/2}\sigma_{4\_3} & II_{\sigma\_3}{}^{(n-1)/2}\sigma_{5\_3} & II_{\sigma\_3}{}^{(n-1)/2}\sigma_{6\_3} \\ II_{\sigma\_4}{}^{(n-1)/2}\sigma_{1\_4} & II_{\sigma\_4}{}^{(n-1)/2}\sigma_{2\_4} & II_{\sigma\_4}{}^{(n-1)/2}\sigma_{3\_4} & II_{\sigma\_4}{}^{(n-1)/2}\sigma_{4\_4} & II_{\sigma\_4}{}^{(n-1)/2}\sigma_{5\_4} & II_{\sigma\_4}{}^{(n-1)/2}\sigma_{6\_4} \\ II_{\sigma\_5}{}^{(n-1)/2}\sigma_{1\_5} & II_{\sigma\_5}{}^{(n-1)/2}\sigma_{2\_5} & II_{\sigma\_5}{}^{(n-1)/2}\sigma_{3\_5} & II_{\sigma\_5}{}^{(n-1)/2}\sigma_{4\_5} & II_{\sigma\_5}{}^{(n-1)/2}\sigma_{5\_5} & II_{\sigma\_5}{}^{(n-1)/2}\sigma_{6\_5} \\ II_{\sigma\_6}{}^{(n-1)/2}\sigma_{1\_6} & II_{\sigma\_6}{}^{(n-1)/2}\sigma_{2\_6} & II_{\sigma\_6}{}^{(n-1)/2}\sigma_{3\_6} & II_{\sigma\_6}{}^{(n-1)/2}\sigma_{4\_6} & II_{\sigma\_6}{}^{(n-1)/2}\sigma_{5\_6} & II_{\sigma\_6}{}^{(n-1)/2}\sigma_{6\_6} \end{bmatrix}$$

In $\underline{\underline{S}}$, σ_{i_j} denotes the ith component of the deviatoric stress in Kelvin notation corresponding to the jth column of $\underline{\underline{E}}$, calculated with the pseudo-Taylor method described by Hansen et al., (2016a), and II_{σ_j} is the second invariant of each stress tensor (corresponding to the jth column of $\underline{\underline{E}}$). Equation (7) needs to be inverted to determine $\underline{\underline{A}}$. However, due to the incompressibility criteria and because $\underline{\underline{S}}$ builds up by deviatoric stresses, $\sum_{i=1}^{3} E_{ij} = 0 \wedge \sum_{i=1}^{3} S_{ij} = 0$ for each j. This means that $\underline{\underline{S}}$ is not invertible in its full form. However, we do not lose information by reducing both $\underline{\underline{E}}$ and $\underline{\underline{S}}$ by one column and one row (the first column and row) because the first component of both the strain rate and the deviatoric stress can be reconstructed from their second and third components. This reduction yields $\underline{\underline{E}}'=\underline{\underline{A}}'*\underline{\underline{S}}'$, where each matrix has 5 rows and columns and a rank of 5. Hence, $\underline{\underline{S}}'$ is invertible, so

$$\underline{\underline{A}}'=\underline{\underline{E}}'*\underline{\underline{S}}'^{-1} \tag{8}$$

can be solved.

Knowing the fluidity parameter tensor, $\underline{\underline{A}}'$, for a given olivine texture allows us to compute the full strain-rate tensor for any given applied stress tensor. The actual deformation that is produced depends on model assumptions about how this deformation is geodynamically expressed in the rock. In this study, we examine geodynamic processes associated with simple shear of the asthenosphere, e.g., as produced by the motion of a surface plate over an asthenospheric layer (Figure 1). To implement this deformation, we impose a deformation gradient consistent with simple shear, for which the deformation tensor ($D_{ij} = \partial u_i/\partial x_j$) is

$$D = \begin{bmatrix} 0 & 2\dot{\varepsilon}_{12} & 2\dot{\varepsilon}_{13} \\ 0 & 0 & 2\dot{\varepsilon}_{23} \\ 0 & 0 & 0 \end{bmatrix} \tag{9}$$

for the case in which the asthenosphere is sheared with force F_1 (Figure 1) and thus driven by a stress σ_{13}. The deformation that results is described in (9) by D_{12}, D_{23}, and D_{13}, where D_{12} and D_{23} are only excited because of the anisotropic nature of the rheology. Note that we neglect the normal strain rate components ($D_{11}=D_{22}=D_{33}=0$) assuming that the volumetric constraints on the system do not permit net elongation or contraction in any direction. From the imposed deformation, we can calculate the associated texture evolution as a function of time for a given applied stress history. The time-step in the calculation is set based on the strain rate to have 0.1 strain increment for each time-step, which we have found to produce stable time results.

2.2 Geodynamic model

To investigate the influence of anisotropic viscous behavior in geodynamic scenarios with changing orientations of stress, we model the deformation of a set of olivine grains representing the behavior of the asthenosphere. We apply a shear stress of 0.68 MPa, which roughly corresponds to a plate of area 6000 km by 6000 km subject to a force of 4.1*10^12 N/m (a lower bound estimate for the value of slab pull force transferred to the plate from the negative buoyancy of a subducting oceanic lithosphere; Schellart, 2004) above a 200 km thick asthenosphere (*Fig. 1A*). We track the deformation of the asthenosphere, using the micromechanical model of texture-development and viscosity anisotropy described above. Based on the anisotropic viscous properties of a representative olivine aggregate, we compute the strain rate within the asthenosphere and associated parameters such as plate speed and movement direction, all as a function of time, accumulated strain, and olivine texture development. To calculate the plate velocity, we assume that the velocity is 0 at the base of the 200-km-thick asthenosphere and that the horizontal velocity at the top of the asthenosphere is the plate velocity.

To investigate different deformation paths that are analogs for a variety of upper mantle processes, we change the orientation of the applied shear stress, and consequently the deformation applied to the asthenosphere, at a chosen instant after an olivine texture has formed (*Fig. 1B*). Such a change could be induced by a change in the external driving forces applied to the asthenosphere. An intuitively simple approach would be to rotate the imposed driving stress relative to the texture that initially formed. However, for numerical and analytical simplicity, we instead rotate the olivine texture with respect to the imposed stress (as shown in *Fig. 1C*), which is held steady. This approach produces an equivalent result and allows us to keep the definition of both the shear stress and the deformation tensors (equation 9) unchanged. Later, we will discuss the geodynamic scenarios represented by the various rotations of the olive texture with respect to the applied shear stress.

We define the angles α and β as the orientations of the imposed shear stress and the resulting plate motion with respect to a coordinate system fixed in the asthenosphere (x-axis, *Fig. 1C*). Thus, α is the angle between the (1)-axis (which is the same as the direction of the shear stress) and the x-axis (which is the angle of rotation of the texture) in *Fig. 1*, and β is the angle between the plate motion direction and the (x)-axis. The horizontal shear components of the strain rate ($\dot{\varepsilon}_{23} \wedge \dot{\varepsilon}_{13}$) are used to calculate the direction of the plate movement (β), as follows:

$$\beta = atan\left(\frac{\dot{\varepsilon}_{23}}{\dot{\varepsilon}_{13}}\right) + \alpha \tag{9}$$

3. Results

We present the results of 27 models with different deformation paths. Each model result is an average of 5 individual runs, each initiated with 1000 olivine grains with initial orientations randomly drawn from a uniform distribution. Therefore, we effectively represent the asthenosphere under a large (6000x6000 km^2) plate using 5*1000 grains.

3.1. Monotonic simple shear

First, we present the evolution of asthenospheric strain rates and olivine texture development from a uniformly distributed texture (i.e., an isotropic mantle) to a well-developed texture (anisotropic, weak mantle). As the mantle accumulates strain, the a-axes of olivine rotate towards the shear direction *(Fig. 1B)*, developing a texture that decreases the effective viscosity of the asthenosphere and, therefore, increases the velocity of the plate. We examined two sets of models differing only in the randomly created uniformly distributed orientations at the start of the models (*Fig. 2*, black and grey curves). The similarity of these two model averages implies that the average of model runs with 5x1000 grains gives a reasonably stable result. However, subtle differences in the initial textures of the two models can still cause minor differences in the amplitudes of the fluidity parameters (*Fig. 2B*).

The strain rate exhibits characteristic variations throughout this deformation (*Fig. 2*)., which result from the texture evolution of the olivine aggregates, and the associated changes in the fluidity parameter tensor (*Fig. 2B and 2C*). With an initially uniform olivine distribution, the strain rate in the asthenosphere is 2.5 10^{-14} s^{-1}, which corresponds to a plate velocity of ~7 cm/yr velocity. As accumulated strain increases, the olivine texture develops, the effective viscosity of the asthenosphere decreases, and the plate velocity increases, reaching a maximum of 10cm/yr ($3.3 \cdot 10^{-14}$ s^{-1}) around a strain of 8, i.e. after ~14 Myr of shearing. With further shearing, the plate velocity decreases and subsequently stabilizes at 8.5 cm/yr ($2.7 \cdot 10^{-14}$ 1/s). The effective viscosity is inversely proportional to the strain rate, reaching a minimum at ~15 Myr (strain of 8) and slightly increases during the later history. The magnitude of the viscosity varies from 2.9-4.5 $x10^{19}$ Pa·s. Hence, with continuous shearing, the lattice preferred orientations of the olivine crystals decrease the asthenosphere's effective viscosity by less than a factor of 2.

Both the normal components of the fluidity tensor (A_{44}, A_{55}, A_{66} in *Fig. 2B*) and the shear components (A_{45} and A_{65} in *Fig. 2C*) exhibit variations with time as the olivine texture develops. The non-zero component of the stress tensor is σ_{13}, (σ_5 in Kelvin notation), which means that A_{55} represents the fluidity in the shear direction. A_{44} and A_{66} represent the values of the fluidity that would control the plate motion rate if we were to change the shear stress to σ_{23} or σ_{12}, respectively. Initially, when there is no preferred orientation of the olivine grains, these three normal fluidity components are the same, but as the asthenosphere deforms and the texture develops, A_{55} increases, which is associated with a decrease in viscosity and an increase in the plate velocity. In contrast, the fluidity component A_{44} (A_{2323}) decreases, which indicates that it would become harder and harder to shear the asthenosphere with σ_{23}. Surprisingly, A_{66} increases with progressive deformation, and most of the time is even larger than A_{55}. Thus, as the texture develops in association with shearing on the (3) plane in the (1) direction, it also becomes easier to shear the asthenosphere along the vertical (*2*) plane in the (3) direction. The A_{45} and A_{65} components (*Fig. 2C*) are noteworthy because these components couple σ_{13} to $\dot{\varepsilon}_{23}$ and $\dot{\varepsilon}_{12}$, respectively (eq. 5). These components are initially zero, but do take on finite values with progressive deformation. In other words, as the anisotropy of the system develops, the applied shear stress begins to induce shear strains on planes other than the primary shear plane, and in directions other than the primary shear direction. However, because these components are two orders of magnitude lower than A_{55}, the strain rate in this simple case is dominated by the effects of A_{55}. Consequently, values of A_{55} (*Fig 2B*), strain rate (*Fig. 2D*), and plate velocity (*Fig. 2D*) all exhibit the same trend as a function of time and strain.

3.1.1. Rheology and texture parameters

As demonstrated above, the plate velocity (calculated from the horizontal strain rate) and the shear-parallel (A_{55}) component of the fluidity tensor are linearly dependent, and those terms are inversely proportional to the effective viscosity. To further understand the initially increasing and subsequently decreasing evolution of the strain rate, the relationship between the texture and the rheological behavior of the asthenosphere (olivine aggregate) needs to be examined. In the literature, a number of texture parameters have been proposed to quantify the orientation distribution of a group of crystals. For example, the J-index (also referred to as the texture strength) provides a metric for the degree of alignment of crystal orientations (Bunge, 1982), varying between 1 (uniform distribution) and infinity (single-crystal texture). The M-index (Skemer et al., 2005) also assesses the degree of alignment and results from the difference between the uncorrelated and the uniform misorientation-angle distributions, with a value between 0 (uniform distribution) and 1 (single-crystal texture). We calculated both the J- and the M- indices with MTEX (Mainprice et al., 2015) and plotted the latter along with the plate velocity against the accumulated strain (*Fig. 3A*). Comparing the two curves (blue and yellow, for the plate velocity and the M-index, respectively), no direct relationship is observable.

We examine the subtleties of the textural development with pole-figures that indicate the orientation distributions of the three main axes of the olivine grains (*Fig.3*). These plots illustrate that better correlation may be found between the plate velocity and the distributions of individual axes instead of the M-index, which describes the orientation distribution of all three axes. For example, as the plate velocity decreases between the strains of 8 and 16, the distributions of the a- and c-axes become more girdled, while the distribution of the b-axes becomes more clustered, resulting in an increasing M-index. Thus, the qualitative comparison of the pole figures with the plate velocity suggests that the distribution of a-axes, which represents the easiest slip direction, exerts a primary influence on the rheological behavior of the aggregate.

Therefore, we calculate three additional parameters that describe the degree to which the orientation distribution is random (*R*), girdle-like (*G*) or point-like (*P*), for each crystallographic axis (a-axes: *P-a, G-a, R-a*; b-axes: *P-b, G-b, R-b*; c-axes *P-c, G-c, R-c*) (Vollmer, 1990). All three parameters vary between 0 and 1, and the sum of all three parameters is 1 for each axis distribution. We plot these texture parameters against the accumulated strain and the plate velocity (*Fig. 3A*), revealing some correlation between the *P-a* values and the plate velocity and some anticorrelation between the *G-a* values and the plate velocity.

3.2. Change in the direction of the shear force

The aim of this section is to test several deformation paths that, to first order, represent those expected for different geodynamic processes. For example, changing the force acting on the plate from the (1) direction to the (2) direction (i.e., from force F_1 to force F_2 in *Fig. 4*) represents a change in the direction of the pull force acting on a tectonic plate, and should change the direction of plate movement (*Fig. 4*). Other changes to the force that we explore are illustrated in Fig. 4. These force directions can mimic shearing induced by subduction initiation and/or dripping (F_3 and F_5) or the start of transform faulting (F_4 and F_6).

First, we describe the results of an instantaneous change in the direction of asthenospheric shear force (from F_1 to F_2, F_3, F_4, F_5, or F_6 in *Fig. 4*). We then examine the influence on the deformation behavior of (1) the rate of rotation of the shear force direction (from 1 Myr/90° to 12 Myr/90°), (2) the amount of texture development prior to the change, and (3) the total rotation angle of the driving stress when switching from F_1 to F_2. As noted above, we implement a change in the driving force (or shear stress) by rotating the textured olivine aggregate (formed by applying the shear of model 1 for a chosen amount of accumulated strain) while keeping the shear stress constant (*Fig. 1C*).

3.2.1 Instantaneous change in shear direction

At a strain of 8 (i.e., after shearing the olivine aggregate for 14 Myr) the a-axes distribution reaches the maximum value of P (*Fig. 3*). Hence, to maximize the effect of anisotropy in our tests, we first reach a shear strain of 8 applying σ_{13} (with the same initial texture as in model 1), followed by a rotation of the aggregate 90° along the x- (representing a change from F_1 to F_4), y- (F_3), z- (F_2), x then y- (F_5) or x then z- axes (F_6). These five types of rotations of the aggregate are equivalent to the five different ways to change the possible shear and deformation directions. As described above, with the change of the effective shear stress orientation the deformation tensor also changes to achieve simple shear created by the modelled forces. Referring to *Fig. 4*, rotating the aggregate around its x or its x then z axes represents shearing along a transform fault (F_4 or F_6), rotation around the y or the x then y axes represents shearing due to dripping or subduction (F_3 or F_5), while rotation around the z axis represents a change in the direction of the horizontal shear (F_2) (e.g., due to a change in the direction of slab pull force).

The effect of changing the shear direction largely depends on the direction of the new shear stress with respect to the textured mantle (*Fig. 5*). For example, when the rotation results in a new shear direction parallel to the (2) direction (F_2 or F_6), the strain rate decreases dramatically, from $3.3 \cdot 10^{-14}$ to $7 \cdot 10^{-15}$ s^{-1} (*Fig. 5A*, *B*, dark blue and green curves). Translating to plate velocity, this change implies a decrease from 13-14 cm/yr to 2-3 cm/yr.

3.2.1.1 Representing change in plate motion direction

Rotating the olivine aggregate around its z-axis represents a relative change in the direction of the plate driving force. The result of a model with 90° instantaneous rotation (*Fig. 5*) exhibits a dramatic decrease in strain rate and a slow recovery of the olivine texture after the rotation. By the end of the model run (total shear strain of 21) the strain rate has increased to $1.9 \cdot 10^{-14}$ s^{-1}, which is still less than the strain rate for the initially isotropic aggregate. Because of the slow deformation associated with the diminished strain rate, this partial recovery took almost 50 Myr. Examination of the change in olivine texture directly after the rotation (*Fig. 5*) shows that the orientations are well organized but that the preferred orientation is perpendicular to the direction of shearing (*Fig. 5*). When the strain rate finally starts to increase, the a-axis distribution is more random or girdle-like rather than point-like, even at a total strain of 21. In *Fig. 5A*, we also present the three fluidity components that determine the total strain rate for the model of instantaneous plate motion change. When the texture is rotated, the A_{55}

component (which relates σ_{13} to $\dot{\varepsilon}_{13}$) decreases while both A_{45} and A_{65} exhibit a minor increase, leading to similar values of all three components.

3.2.1.2 Shear forces associated with transform faults

There are two possibilities for creating shear stress along a vertical plane in a rough approximation of the stress state associated with a transform fault. The possible shear forces are F_4 or F_6 (*Fig. 4*), which produce very different paths in the strain-rate evolution (*Fig. 5B*) if there is already a well-developed texture associated with deformation due to F_1. From the time of rotation (at a strain of 8), the two models diverge. In *Fig. 5B*, representing the switch from shearing with F_1 to F_4 (i.e. texture rotation around the x-axis), the purple curve exhibits an increase in strain rate right after the rotation (to $4.6{\cdot}10^{-14}$ s^{-1}), which then decreases until $2.2{\cdot}10^{-14}$ s^{-1}. Representing the switch from shearing with F_1 to shearing with F_6 (i.e. texture rotation first along the x axes and then along the z axes), the dark blue curve on Fig. 5B exhibits a decrease in strain rate to $7{\cdot}10^{-15}$ s^{-1} and then slowly recovers over the next 20-25 Myr (by a total strain of 14). Notably, the two paths do not converge at high strain, but rather, the initially weakest scenario (F_4) becomes the strongest at high strain, and vice versa. The crossover of the two models is related to their different textural development. Switching from F_1 to F_6 results in a point-like distribution of the a-axes perpendicular to the shear direction. With subsequent strain, this distribution first becomes more uniformly organized, before reforming a point-like distribution in the new shear direction that is more strongly aligned than the distribution prior to the change in shear direction. In contrast, changing from F_1 to F_4 (rotation around the x-axes) keeps the a-axes distribution basically aligned with the shear direction. With subsequent strain, the a-axes distribution forms a girdle, decreasing the initial point-like distribution and leading to slower strain rates than prior to the change in shear direction.

3.2.1.3 Shear forces associated with dripping/subduction

There are two possibilities for creating shear stress in a vertical direction as a rough approximation of the stress state associated with subduction or dripping. Changing from F_1 to F_3 (texture rotation around the y-axis; *Fig. 4*), results in an initial decrease in strain rate (i.e. small increase in the effective viscosity) (*Fig. 5C*, cyan curve) followed by a period with increasing strain rate, between strains of 8.5 (0.5 after the switch) to 13, peaking at $9.4{\cdot}10^{-14}$ s^{-1}. The model shows a decreasing trend in strain rate immediately after its peak, reaching a final strain rate of $2.8 \cdot 10^{-14}$ s^{-1} (after a total strain of 21). In contrast, changing from F_1 to F_5 is relatively easy, as the model exhibits an increase in strain rate associated with the rotation (*Fig. 5C,* orange curve). This model shows a quicker and greater increase, and has a peak strain rate ($8.1 \cdot 10^{-14}$ s^{-1}) already 3 strain units after the rotation. The peak follows with a quickly decreasing strain rate that stabilizes around ~$2.8 \cdot 10^{-14}$ s^{-1}, which is the same as the strain rate for larger strains in reference model 1 (black curve). Similar to the "transform fault" models, the strain-rate curves for "subduction/dripping" can be linked to the texture development. The higher strain rate in the model applying F_5 (x- then y- rotation) compared to the model applying F_3 results from a more point-like distribution of the olivine a-axes at the peak strain rate (at a strain of 12)(*Fig. 5C*).

3.2.2. Rate of rotation of the stress orientation

In the preceding section, the change in texture orientation relative to the applied forces was instantaneous. In the following sections, the rate, timing, and amount of rotation of the olivine aggregate are examined. Here we focus on the simplest case, a change in the plate-motion direction (F_1 changing to F_2). Here, we impose a 90° rotation over a time interval ranging from 1 to 13 Myr, after ~14 Myr of initial shearing (an accumulated strain of 8).

As described above, we use α and β (eq. 9) to indicate the angle between the x-axis (in the aggregate reference frame) and the shear force and plate motion directions, respectively. During rotation of the aggregate, α linearly changes with time from 0° to -90°. In contrast, the angle β does not change linearly with time and can differ from α significantly because the olivine texture excites plate motion differently in varied directions. During the rotation period, and independently of its duration, the plate movement differs from the shear direction by up to 20° (*Fig. 6a*). Minor differences can be observed depending on the rotation rate. Once 90° rotation is achieved, the plate movement is either parallel to the shear direction (1 and 10 Myr rotation period), overturned (3 and 5 Myr rotation period) or rotated less than the shear direction (13 Myr rotation period). After rotation, all models evolve in a similar manner, resulting in velocity vectors 15-20° away from the shear direction. The plate speed drastically decreases, reaching 2 cm/yr by the end of the rotation period (*Fig. 6b*). As in the instantaneous rotation model, the plate movement cannot recover its original rate after the rotation (*Fig. 6b*). The models with shorter rotation time (1-5 Myr) reach a maximum of 4.7 cm/yr while the models with longer texture rotation time (10-13 Myr) reach a maximum of 3.7 cm/yr by the end of the model (at strain ~ 20-21). Interestingly, during the first ~4° of rotation, the plate velocity increases, except for the model with 1 Myr rotation time, where the rotation step is 9°/timestep (as the timestep is fixed to 100 kyr during the rotation). This increase can be explained by the mean orientation of the olivine texture (see pole figures for a strain of 8 on Fig. 3) and the plate movement (*Fig. 6A*) before the onset of rotation, which are both a few degrees (~ 4° and -1.2°, resp.) offset from the shear direction. Hence, at the onset of rotation, the texture initially becomes more aligned with the shearing, resulting in up to 2 cm/yr increase in the plate velocity (see texture evolution animations, which are available in the supplementary materials for each model).

3.2.3. Role of texture evolution prior to the rotation

In an additional series of calculations, we varied the amount of accumulated strain between 2 and 14 prior to a 90° rotation, which was implemented using two different rotation rates (90° and 9°/Myr).

The magnitude of the velocity decrease associated with rotation depends on the maturity of the olivine texture prior to rotation. Thus, the magnitude of the velocity decrease is inversely correlated with the amount of strain on the aggregate before rotation (*Fig. 7B and D*). However, the rate of rotation has only a small effect, as described previously (*Fig. 6*). Note that in the models in which the rotation is imposed after a strain of 11 or 14, faster rotation results in a slightly lower minimum plate velocity (*Fig. 7D*). Only the model with fast and early rotation (rotation at a strain of 2) exhibits velocities that return to the original plate velocity magnitude, while the other models reach strain of 21 with only 3.5-6 cm/yr plate velocity (Fig. 7B).

A large range of variation in the plate motion direction can be observed depending on the amount of initial strain, rotation rate, and time/total accumulated strain (*Fig. 7A & C*). In most of the models, the difference α-β grows from ~-1° to ~15-20° during rotation (see the two outlined circles in each line on *Fig.7C*), which is also the maximum difference between α and β. There are three slight outlier models, in which extreme magnitudes of α-β occur during the model evolution. With an initial strain of 5 and a slow-rotation rate, the plate motion direction can differ from the shear direction by up to 29°, while in the models in which an initial strain of 14 is imposed, the plate-motion direction rotates more than the shear direction, reaching extremes of -6 ° and -21° (with 1 and 10 Myr rotation time, respectively).

3.2.4. Role of the amount of rotation

In more realistic geodynamic scenarios, the driving forces on plates are unlikely to rotate as much as 90°, so we additionally tested a range of rotations from 22° to 90° degrees with slow

(9°/Myr) and fast (90°/Myr) rotation rates. In all of these models, the aggregate was sheared with force F_1 until a strain of 8 prior to the rotation. We found (*Fig. 8*) that the larger the rotation, the lower the average strain rate, and therefore the lower the average plate velocity (*Fig. 8B & 8D*). Furthermore, the models with faster rotation rates exhibit a greater variability of plate motion directions and velocities than the models with slower rotation rates (*Fig. 8*). With only 22° rotation, β differs from α by only 15° during the rotation in both models, and this difference linearly decreases as the model progresses until, at the end of the model, the plate motion becomes parallel to the shear direction. The plate velocity decreases to 5.4-5.1 cm/yr, which then climbs back to the isotropic rate (~7.2 cm/yr) by the end of the models. If the total change in shear direction is 45° or more, all models result in ~20° difference between α and β during the rotation, independent of the rate of rotation. Later, the models with slower rotation rate result in even larger differences between α and β. The plate motion direction can change more quickly if the plate velocity is high, such as in the model with 45° rotation at 90°/Myr during the period between 25 and 35 Myr (*Fig. 8B*). On the other hand, in the model with 67° rotation at 9°/Myr, the plate velocity remains between 2-4 cm/yr, and α-β remains ~20° (15-25°).

4. *Discussion*

The results described above suggest that the effective viscosity and strain rate of the asthenosphere, and the associated plate velocity at the surface, are extremely sensitive to the olivine texture. The asthenosphere weakens as the olivine texture develops with the a-axes parallel to the shear direction (‘anisotropic weak’ on *Fig. 1B*), allowing for a 40% increase in plate velocity (or equally, decrease in effective viscosity). The asthenosphere acts ‘strong’ (*Fig. 1C*) if the mean a-axes direction is perpendicular to the shear direction. In this case, the effective viscosity is up to ~5 times higher than if the a-axes are parallel to the shear force, resulting in a slower plate velocity that is only a third of the velocity over the isotropic asthenosphere and a fifth of that in the ‘anisotropic weak’ case (Fig. 10). The evolution of the plate velocity and plate-motion direction (or the entire matrix of $\dot{\varepsilon}$) is a function of the olivine texture, which evolves due to the deformation. Hence the asthenospheric rheology depends on the kinematics and vice-versa.

Without changes in the shear force direction, the plate-velocity evolution follows a similar trend to the values of *P-a* (point-like distribution value for the olivine a-axes) (*Fig. 3*). However, if the direction of the shear force changes, this correlation is less clear. We calculated the texture parameters described in section 3.1.1 for each model for a 0.5 strain increment, for which an example is presented in *Figure 9*. If the texture is rotated 90° with respect to the shear stress (in 1 Myr), then the changes in the values of *P*-a are no longer correlated to the changes in the plate velocity, especially around the time of the rotation (between a strain of 8 and 11), at which point the values of *P* for the a-, b-, and c-axes (*P-a, P-b, P-c*) and the M-index are the largest (*Fig. 9*), while the plate velocity is the lowest.

To analyze the overall relationship between texture parameters and kinematic parameters (e.g. plate velocity), we performed a Pearce correlation for all the models representing shearing by plate pull. The correlation values between the plate velocity and texture parameters (*Fig. 9*) demonstrate that the mean orientation of the olivine a-axes (*ori-a* on *Fig. 9*) as well as the mean orientation of the c-axes (*ori-c*) are highly anticorrelated with the plate velocity. In contrast, *P-a* has the highest correlation with the plate velocity of 0.64, which is similar to the strength of the anticorrelation between the G-value (girdle-like distribution) of the a-axes (*G-a*) and the plate velocity (v_{plate}). It is important to note that these parameters are not independent from each other, as *G-a* and *P-a* are anticorrelated with a coefficient of -0.94 (similarly, -0.83 between *G-b* and *P-b*) and a 0.85 correlation between *ori-a* and *ori-c* (*Suppl. Fig. S1*). Based on the correlation between the texture parameters and the plate velocity, as well as between each pair of texture parameters, we find that the plate velocity can be linked essentially to two parameters, the mean orientation and the value of *P* for the distribution of the a-axes of the olivine grains, and therefore we see the strongest correlation between the plate velocity and the product of those two parameters (*P-a ·cos(ori-a) in Figure 9*).

The orientation of the olivine grains also exerts an important control on the direction of the plate motion. While the relationship between these factors is not straightforward, it is clear that as *ori-a* starts to differ from the shear direction, there is a corresponding change in the plate-motion direction (*Fig. 7 & 8*). The highest values of β (plate-motion direction) occur at times in which *ori-a* differs 30-60° from the shear direction. When this angle is higher, β decreases to ~0°, and the plate velocity slows considerably. This behavior occurs because it is not possible to create strain perpendicular to the forcing. Thus, when a grain is oriented such that the a-axis is perpendicular to the shear direction, the easiest slip system cannot be activated (*Suppl. Fig. S2*).

5. *Application to natural phenomena*

Our experiments suggest that mantle anisotropy exerts a range of different viscous responses to different tectonic processes (*Fig. 10*). Depending on the orientation of the tectonic force, the anisotropic texture may either assist or resist continued deformation, which means that certain types of tectonic process may be preferred over others.

5.1 Change in the direction of plate motion

By changing the orientation of the shear force in the horizontal direction (e.g. *Fig. 5A*), we demonstrate that the asthenospheric texture exerts a significant influence on the motion of a tectonic plate. Indeed, the effective viscosity of an olivine aggregate may be a factor of ~5 times smaller when the shear force is parallel to the mean orientation of the a-axis of olivine grains (*ori-a*) compared to perpendicular to *ori-a* (Fig. 5A). Thus, if the texture beneath the plate is characterized by strong alignment of the a-axes, then a large change in the orientation of forces on the plate may result in a significant slowing of the plate velocity (up to a factor of 5), even if the change in the orientation of forces occurs over a period of more than 10 million years (*Fig. 6*). The stronger the initial texture (e.g., formed as a result of strains greater than 2, *Fig. 7*), and the larger the change in the orientation of the plate driving force (e.g., more than 45°, *Fig. 8*), the larger and more lasting the asthenospheric resistance will be to changes in the orientation of the driving forces. This asthenospheric resistance, induced by shear forces misaligned with the preferred orientation of the texture, can also result in plate motion that is not parallel to the plate driving force (*Figs. 6A, 7A, 8A*). This misalignment can last for 10s of millions of years because the asthenospheric texture may be slow to redevelop.

Thus, we expect that anisotropic viscosity may significantly modify the relationship between plate motions and the forces that drive them (e.g., Becker et al., 2006; Conrad and Lithgow-Bertelloni, 2004). Although Becker and Kawakatsu (2011) found that mantle flow models that included viscosity anisotropy behaved similarly to isotropic models, their study did not examine time-dependent behavior. Instead, our results suggest that time-dependent changes to the driving forces on plates, or to the amplitude or orientation of the anisotropic texture beneath them, should result in potentially large differences between the orientation of the net driving force on a plate and the direction of the resulting asthenospheric flow and plate motion. The effective viscosity of the asthenosphere may also vary spatially beneath the plate depending on the orientation and maturity of the olivine texture locally. These spatial, temporal, and directional differences in the resistance that the asthenosphere exerts on plate motions may persist for durations of 10s of Myr (e.g., *Fig. 8*).

Our results suggest that anisotropic viscosity may cause a plate to respond only sluggishly to changes in the direction of its driving forces. This effect occurs because the anisotropic texture beneath the plate slows plate motions in directions at an angle to the preferred direction of the olivine texture (*Fig. 8*), but also requires strains of at least 2-4 to begin re-orienting into a new direction (*Fig. 7*). Indeed, plate motions in global plate reconstruction models are observed to remain relatively stable for long periods (10s of Myr), except for a few brief periods of global reorganization (Bercovici et al., 2000). This overall stability has been attributed to slow evolution of the plate driving forces (e.g., Richards and Lithgow-Bertelloni, 1996), despite the possibility that slab breakoff (Andrews and Billen, 2009) or even a change in the direction and magnitude of subduction-related stresses (e.g., Capitanio et al., 2011; Jahren et al., 2005) may change the driving forces on plates quickly. Our results suggest that the sluggishness with which anisotropic textures adjust to changes in the orientation of the applied driving force may represent an alternative mechanism to explain the gradual changes in the direction of plate motions observed in reconstructions. This mechanism predicts that driving forces and plate motions may be misaligned for significant periods of time, and indeed such misalignment might be currently observed in the Pacific. Based on a reconstruction of the plate driving force and the plate velocity in the centroid of the Pacific plate, Faccenna et al., (2012) showed that, in the last 20 Myr, the Pacific plate moved with an ~15° degree offset with respect to the calculated driving force. Although the history of plate motion for the Pacific basin is more complicated and involves varying shear orientation and texture maturity beneath the Pacific plate, this directional difference is consistent with our modelling results. In particular, we find differences of up to 30°, but more often 10-20°, between the force and strain directions after a change in the forcing direction is applied (*Fig. 8C*).

5.2 Oceanic transform faults

Our results demonstrate that shear stresses in a horizontal direction on vertical planes, as expected in association with motion on transform faults, should lead to enhanced strain rates if the shearing direction is parallel to the plate motions that generated the asthenospheric texture (F_4 in *Fig. 4*), or diminished strain rates for transform motion perpendicular to this texture (F_6 in *Fig. 4*; *Fig. 5B; Fig. 10*). Interestingly, the results of this simple approach are consistent with the general orientation of transform faults on oceanic plates, even though such faults usually form close to the ridge where the asthenosphere has not been sheared for long, and where texture development involves a more complicated history associated with corner flow (Blackman et al., 2017). Mantle textures should not resist, and might even augment the elongation of transform faults, and perhaps allow for long and slowly-slipping "megatransforms" (Ligi et al., 2002). Indeed, we note that transform faults are nearly always strike slip in nature, and oriented perpendicular to ridge spreading, despite sometimes unfavorable stress orientations to produce this type of deformation (Hensen et al., 2019). It is possible that the asthenospheric textures developed by plate motion, for which the mean a-axis direction is presumably oriented perpendicular to ridges, serve to guide transform faults into this orientation. The interaction between lithospheric stresses, asthenospheric anisotropy, and transform fault formation and development, are still poorly understood (Gerya, 2016).

5.3 Initiation of subduction or dripping

Changing the direction of the shear force from horizontal to vertical roughly represents the initiation of slab subduction or dripping of lithospheric mantle. Our results (*Fig. 5C, Fig. 10*) suggest that asthenosphere with well-oriented olivine grains imposes little resistance for such processes. Motion in response to a vertically-oriented shear force on a plane perpendicular to the initial direction plate-motion (e.g, trench-perpendicular subduction, F_3 in *Figure 4*) exhibits a short period of increased resistance to deformation that must be overcome before the texture weakens (*Figure 5C*, blue curve). Thus, asthenospheric textures may initially pose a slight impediment to subduction initiation, but after a few Myrs, the olivine texture evolution may hasten the evolution of subduction. In contrast, vertical motion in response to a vertical shear force on a plane parallel to plate motions (e.g., very oblique subduction or Richter-rolls, F_1 to F_5 in *Fig. 4*) is initially favored by the anisotropic fabric, and additional fabric weakening may allow for accelerated growth of lithospheric instabilities (*Fig. 5C*, orange curve). Indeed, sub-lithospheric instabilities, for example in the Pacific basin (Ballmer et al., 2009), generally align parallel to the plate motion direction. Although this alignment is observed in numerical models of small-scale convection without asthenospheric textures (Ballmer et al., 2007), our study predicts that anisotropic viscosity should enhance the directionality of such instabilities.

However, both subduction initiation and small-scale convection involve more complex deformation than the simple instantaneous change in shear direction that is modeled here, and the rheology of the lithosphere plays a potentially larger role. Furthermore, it is possible that olivine texture can become frozen into the oceanic lithosphere as it cools (Tommasi, 1998), which would likely affect the rheology of the plate, and hence, its resistance to bending. Although analysis of this deformation is beyond the scope of this study, the combined effect of asthenospheric and lithospheric weakening due to anisotropy could allow for subduction zone initiation in response to lower tectonic stresses than usually expected (e.g., Gurnis et al., 2004). To explore the role of asthenospheric and lithospheric viscous anisotropy in such complex processes, more complex 3D geodynamic modeling is required.

It is worth mentioning that the model we apply for stresses related to subduction initiation or gravitational instabilities after plate motion can be equally applied to situations in which vertical shearing precedes horizontal shearing, such as at mid ocean ridges, plume head arrival beneath the lithosphere, or other mantle upwellings. However, previous studies have demonstrated that, at mid-ocean ridges, relatively small strains are associated with the upwelling, and hence, no significant texture is predicted prior the horizontal shearing (Blackman et al., 2017; Kaminski and Ribe, 2002).

6. *Conclusions*

Olivine texture development in the asthenosphere and its response to shearing are highly coupled and can exert considerable influences on geodynamic processes. In response to unidirectional shearing of the asthenosphere, the formation of an olivine texture causes a significant decrease in effective mantle viscosity after accumulating a shear strain of ~5. After this texture has formed, changes to the direction of the forces on the system, as induced by a change in the tectonic setting, result in a different effective viscosity because of the mechanically anisotropic nature of the textured asthenosphere. If the new shear direction is parallel to the mean orientation of the olivine c-axis, which represents the hardest slip system, then the effective viscosity will increase. This is the case for a change in the direction of plate motion or transform motion perpendicular to plate motions. In contrast, the mantle should remain weak, or even become weaker, for shear forces parallel to the a-axis, as for transform motion parallel to plate motions, or the b-axis, as for subduction or convective instability. We find that differences in the effective viscosity associated with shearing asthenosphere across its weak versus strong directions can be over an order of magnitude. These changes to the effective viscosity should hinder some tectonic processes and foster others, depending on their sense of deformation relative to asthenospheric textures (*Fig. 10*). In particular, we expect asthenospheric textures to significantly slow changes to the direction of plate motions and prevent the formation of ridge-parallel transform faults. In addition, these fabrics should assist in the initiation of new subduction zones, accelerate convective instability beneath the lithosphere, and promote the development of transform faults perpendicular to ridges. To fully understand the impact of anisotropic viscosity on plate tectonics and asthenospheric dynamics, olivine fabric development, and the anisotropic viscosity that is associated with it, needs to be integrated into 3D dynamic models of the relevant processes.

Acknowledgement

This work was supported by the Research Council of Norway Centres of Excellence project 223272. Data and code availability: https://doi.org/10.11582/2020.00027 (Please also refer to the supplementary material for more information about the model data and code).

References

Andrews, E.R., Billen, M.I., 2009. Rheologic controls on the dynamics of slab detachment. Tectonophysics, Interpreting the tectonic evolution of Pacific Rim margins using plate kinematics and slab window volcanism 464, 60–69. https://doi.org/10.1016/j.tecto.2007.09.004

Ballmer, M.D., Hunen, J. van, Ito, G., Bianco, T.A., Tackley, P.J., 2009. Intraplate volcanism with complex age-distance patterns: A case for small-scale sublithospheric convection. Geochemistry, Geophysics, Geosystems 10. https://doi.org/10.1029/2009GC002386

Ballmer, M.D., Hunen, J. van, Ito, G., Tackley, P.J., Bianco, T.A., 2007. Non-hotspot volcano chains originating from small-scale sublithospheric convection. Geophysical Research Letters 34. https://doi.org/10.1029/2007GL031636

Bamford, D., Crampin, S., 1977. Seismic anisotropy - the state of the art. Geophysical Journal Of The Royal Astronomical Society 49, 1–8. https://doi.org/10.1111/j.1365-246X.1977.tb03697.x

Becker, T.W., 2008. Azimuthal seismic anisotropy constrains net rotation of the lithosphere. Geophys. Res. Lett. 35, L05303. https://doi.org/10.1029/2007GL032928

Becker, T.W., Chevrot, S., Schulte-Pelkum, V., Blackman, D.K., 2006. Statistical properties of seismic anisotropy predicted by upper mantle geodynamic models. Journal of Geophysical Research: Solid Earth 111. https://doi.org/10.1029/2005JB004095

Becker, T.W., Conrad, C.P., Schaeffer, A.J., Lebedev, S., 2014. Origin of azimuthal seismic anisotropy in oceanic plates and mantle. Earth and Planetary Science Letters 401, 236–250. https://doi.org/10.1016/j.epsl.2014.06.014

Becker, T.W., Kawakatsu, H., 2011. On the role of anisotropic viscosity for plate-scale flow. Geophysical Research Letters 38, 1–5. https://doi.org/10.1029/2011GL048584

Becker, T.W., Kellogg, J.B., Ekström, G., O'Connell, R.J., 2003. Comparison of azimuthal seismic anisotropy from surface waves and finite strain from global mantle-circulation models. Geophys J Int 155, 696–714. https://doi.org/10.1046/j.1365-246X.2003.02085.x

Becker, T.W., Kustowski, B., Ekström, G., 2008. Radial seismic anisotropy as a constraint for upper mantle rheology. Earth and Planetary Science Letters 267, 213–227. https://doi.org/10.1016/j.epsl.2007.11.038

Behn, M.D., Conrad, C.P., Silver, P.G., 2004. Detection of upper mantle flow associated with the African Superplume. Earth and Planetary Science Letters 224, 259–274. https://doi.org/10.1016/j.epsl.2004.05.026

Bercovici, D., Ricard, Y., Richards, M.A., 2000. The Relation between mantle dynamics and plate tectonics: A Primer, in: Richards, M.A., Gordon, R.G., van der Hilst, R.D. (Eds.), Geophysical Monograph Series. American Geophysical Union, Washington, D. C., pp. 5–46. https://doi.org/10.1029/GM121p0005

Blackman, D.K., Boyce, D.E., Castelnau, O., Dawson, P.R., Laske, G., 2017. Effects of crystal preferred orientation on upper-mantle flow near plate boundaries: rheologic feedbacks and seismic anisotropy. Geophysical Journal International 210, 1481–1493. https://doi.org/10.1093/gji/ggx251

Bunge, H., 1982. Texture Analysis in Materials Science: Mathematical Models. Butterworths, London.

Capitanio, F.A., Faccenna, C., Zlotnik, S., Stegman, D.R., 2011. Subduction dynamics and the origin of Andean orogeny and the Bolivian orocline. Nature 480.

Christensen, N.I., 1984. The magnitude, symmetry and origin of upper mantle anisotropy based on fabric analyses of ultramafic tectonites. Geophysical Journal International 76, 89–111. https://doi.org/10.1111/j.1365-246X.1984.tb05025.x

Christensen, U.R., 1987. Some geodynamical effects of anisotropic viscosity. Geophysical Journal of the Royal Astronomical Society 91, 711–736. https://doi.org/10.1111/j.1365-246X.1987.tb01666.x

Conrad, C.P., Behn, M.D., 2010. Constraints on lithosphere net rotation and asthenospheric viscosity from global mantle flow models and seismic anisotropy: ANISOTROPY AND LITHOSPHERE NET ROTATION. Geochem. Geophys. Geosyst. 11, n/a-n/a. https://doi.org/10.1029/2009GC002970

Conrad, C.P., Lithgow-Bertelloni, C., 2004. The temporal evolution of plate driving forces: Importance of “slab suction” versus “slab pull” during the Cenozoic. Journal of Geophysical Research B: Solid Earth 109, 1–14. https://doi.org/10.1029/2004JB002991

Dellinger, J., Vasicek, D., Sondergeld, C., 1998. Kelvin Notation for Stabilizing Elastic-Constant Inversion. Revue de l’Institut Français du Pétrole 53, 709–719. https://doi.org/10.2516/ogst:1998063

Durham, W.B., Goetze, C., 1977. Plastic flow of oriented single crystals of Olivine 1. Mechanical Data. Journal of Geophysical Research 82, 5737–5753.

Eakin, C.M., Rychert, C.A., Harmon, N., 2018. The Role of Oceanic Transform Faults in Seafloor Spreading: A Global Perspective From Seismic Anisotropy. Journal of Geophysical Research: Solid Earth 123, 1736–1751. https://doi.org/10.1002/2017JB015176

Faccenna, C., Becker, T.W., Lallemand, S., Steinberger, B., 2012. On the role of slab pull in the Cenozoic motion of the Pacific plate. Geophysical Research Letters 39, 1–6. https://doi.org/10.1029/2011GL050155

Gaboret, C., Forte, A.M., Montagner, J.-P., 2003. The unique dynamics of the Pacific Hemisphere mantle and its signature on seismic anisotropy. Earth and Planetary Science Letters 208, 219–233. https://doi.org/10.1016/S0012-821X(03)00037-2

Gerya, T.V., 2016. Origin, Evolution, Seismicity, and Models of Oceanic and Continental Transform Boundaries, in: Plate Boundaries and Natural Hazards. American Geophysical Union (AGU), pp. 39–76. https://doi.org/10.1002/9781119054146.ch3

Gurnis, M., Hall, C., Lavier, L., 2004. Evolving force balance during incipient subduction. Geochemistry, Geophysics, Geosystems 5. https://doi.org/10.1029/2003GC000681

Hansen, L.N., Conrad, C.P., Boneh, Y., Skemer, P., Warren, J.M., Kohlstedt, D.L., 2016a. Viscous anisotropy of textured olivine aggregates: 2. Micromechanical model. Journal of Geophysical Research: Solid Earth 121, 7137–7160. https://doi.org/10.1002/2016JB013304

Hansen, L.N., Warren, J.M., Zimmerman, M.E., Kohlstedt, D.L., 2016b. Viscous anisotropy of textured olivine aggregates, Part 1: Measurement of the magnitude and evolution of anisotropy. Earth and Planetary Science Letters 445, 92–103. https://doi.org/10.1016/j.epsl.2016.04.008

Hansen, L.N., Zimmerman, M.E., Kohlstedt, D.L., 2012. Laboratory measurements of the viscous anisotropy of olivine aggregates. Nature 492, 415–418. https://doi.org/10.1038/nature11671

Hensen, C., Duarte, J.C., Vannucchi, P., Mazzini, A., Lever, M.A., Terrinha, P., Géli, L., Henry, P., Villinger, H., Morgan, J., Schmidt, M., Gutscher, M.-A., Bartolome, R., Tomonaga, Y., Polonia, A., Gràcia, E., Tinivella, U., Lupi, M., Çağatay, M.N., Elvert, M., Sakellariou, D., Matias, L., Kipfer, R., Karageorgis, A.P., Ruffine, L., Liebetrau, V., Pierre, C., Schmidt, C., Batista, L., Gasperini, L., Burwicz, E., Neres, M., Nuzzo, M., 2019. Marine Transform Faults and Fracture Zones: A Joint Perspective Integrating Seismicity, Fluid Flow and Life. Front. Earth Sci. 7. https://doi.org/10.3389/feart.2019.00039

Jahren, A.H., Conrad, C.P., Arens, N.C., Mora, G., Lithgow-Bertelloni, C., 2005. A plate tectonic mechanism for methane hydrate release along subduction zones. Earth and Planetary Science Letters 236, 691–704. https://doi.org/10.1016/j.epsl.2005.06.009

Kaminski, É., Ribe, N.M., 2002. Timescales for the evolution of seismic anisotropy in mantle flow. Geochemistry, Geophysics, Geosystems 3, 1–17. https://doi.org/10.1029/2001GC000222

Karato, S., 1987. Seismic anisotropy due to lattice preferred orientation of minerals: Kinematic or dynamic?, in: Manghnani, M.H., Syono, Y. (Eds.), Geophysical Monograph Series. American Geophysical Union, Washington, D. C., pp. 455–471. https://doi.org/10.1029/GM039p0455

Karato, S., Wu, P., 1993. Rheology of the Upper Mantle: A Synthesis. Science 260, 771–778.

Lev, E., Hager, B.H., 2011. Anisotropic viscosity changes subduction zone thermal structure. Geochemistry, Geophysics, Geosystems 12. https://doi.org/10.1029/2010GC003382

Lev, E., Hager, B.H., 2008. Rayleigh-Taylor instabilities with anisotropic lithospheric viscosity. Geophysical Journal International 173, 806–814. https://doi.org/10.1111/j.1365-246X.2008.03731.x

Ligi, M., Bonatti, E., Gasperini, L., Poliakov, A.N.B., 2002. Oceanic broad multifault transform plate boundaries. Geology 30, 11–14. https://doi.org/10.1130/0091-7613(2002)030<0011:OBMTPB>2.0.CO;2

Long, M.D., 2013. Constraints on Subduction Geodynamics From Seismic Anisotropy. Reviews of Geophysics 51, 76–112. https://doi.org/10.1002/rog.20008

Long, M.D., Becker, T.W., 2010. Mantle dynamics and seismic anisotropy. Earth and Planetary Science Letters 297, 341–354. https://doi.org/10.1016/j.epsl.2010.06.036

Mainprice, D., Bachmann, F., Hielscher, R., Schaeben, H., 2015. Descriptive tools for the analysis of texture projects with large datasets using MTEX : strength, symmetry and components. Geological Society, London, Special Publications 409, 251–271. https://doi.org/10.1144/SP409.8

Mühlhaus, H.-B., Čada, M., Moresi, L., 2003. Anisotropic Convection Model for the Earth’s Mantle, in: Sloot, P.M.A., Abramson, D., Bogdanov, A.V., Gorbachev, Y.E., Dongarra, J.J., Zomaya, A.Y. (Eds.), Computational Science — ICCS 2003. Springer Berlin Heidelberg, Berlin, Heidelberg, pp. 788–797. https://doi.org/10.1007/3-540-44863-2_77

Mühlhaus, H.-B., Moresi, L., Hobbs, B., Dufour, F., 2002. Large Amplitude Folding in Finely Layered Viscoelastic Rock Structures. Pure and Applied Geophysics 159, 2311–2333. https://doi.org/10.1007/s00024-002-8737-4

Pouilloux, L., Kaminski, E., Labrosse, S., 2007. Anisotropic rheology of a cubic medium and implications for geological materials. Geophysical Journal International 170, 876–885. https://doi.org/10.1111/j.1365-246X.2007.03461.x

Richards, M.A., Lithgow-Bertelloni, C., 1996. Plate motion changes, the Hawaiian-Emperor bend, and the apparent success and failure of geodynamic models. Earth and Planetary Science Letters 137, 19–27. https://doi.org/10.1016/0012-821X(95)00209-U

Schellart, W.P., 2004. Kinematics of subduction and subduction-induced flow in the upper mantle. Journal of Geophysical Research B: Solid Earth 109, 1–19. https://doi.org/10.1029/2004JB002970

Silver, P.G., 1996. SEISMIC ANISOTROPY BENEATH THE CONTINENTS: Probing the Depths of Geology. Annu. Rev. Earth Planet. Sci. 24, 385–432. https://doi.org/10.1146/annurev.earth.24.1.385

Skemer, P., Katayama, I., Jiang, Z., Karato, S., 2005. The misorientation index: Development of a new method for calculating the strength of lattice-preferred orientation. Tectonophysics 411, 157–167. https://doi.org/10.1016/j.tecto.2005.08.023

Stixrude, L., Lithgow-Bertelloni, C., 2005. Mineralogy and elasticity of the oceanic upper mantle: Origin of the low-velocity zone. Journal of Geophysical Research: Solid Earth (1978–2012) 110. https://doi.org/10.1029/2004JB002965

Tanimoto, T., Anderson, D.L., 1984. Mapping convection in the mantle. Geophysical Research Letters 11, 287–290. https://doi.org/10.1029/GL011i004p00287

Taylor, G.I., 1938. Plastic Strain in Metals. Journal of Inst. Met. 62.

Tommasi, A., 1998. Forward modeling of the development of seismic anisotropy in the upper mantle. Earth and Planetary Science Letters 160, 1–13. https://doi.org/10.1016/S0012-821X(98)00081-8

Vollmer, F.W., 1990. An application of eigenvalue methods to structural domain analysis. Bulletin of the Geological Society of America 102, 786–791. https://doi.org/10.1130/0016-7606(1990)102<0786:AAOEMT>2.3.CO;2

Figures

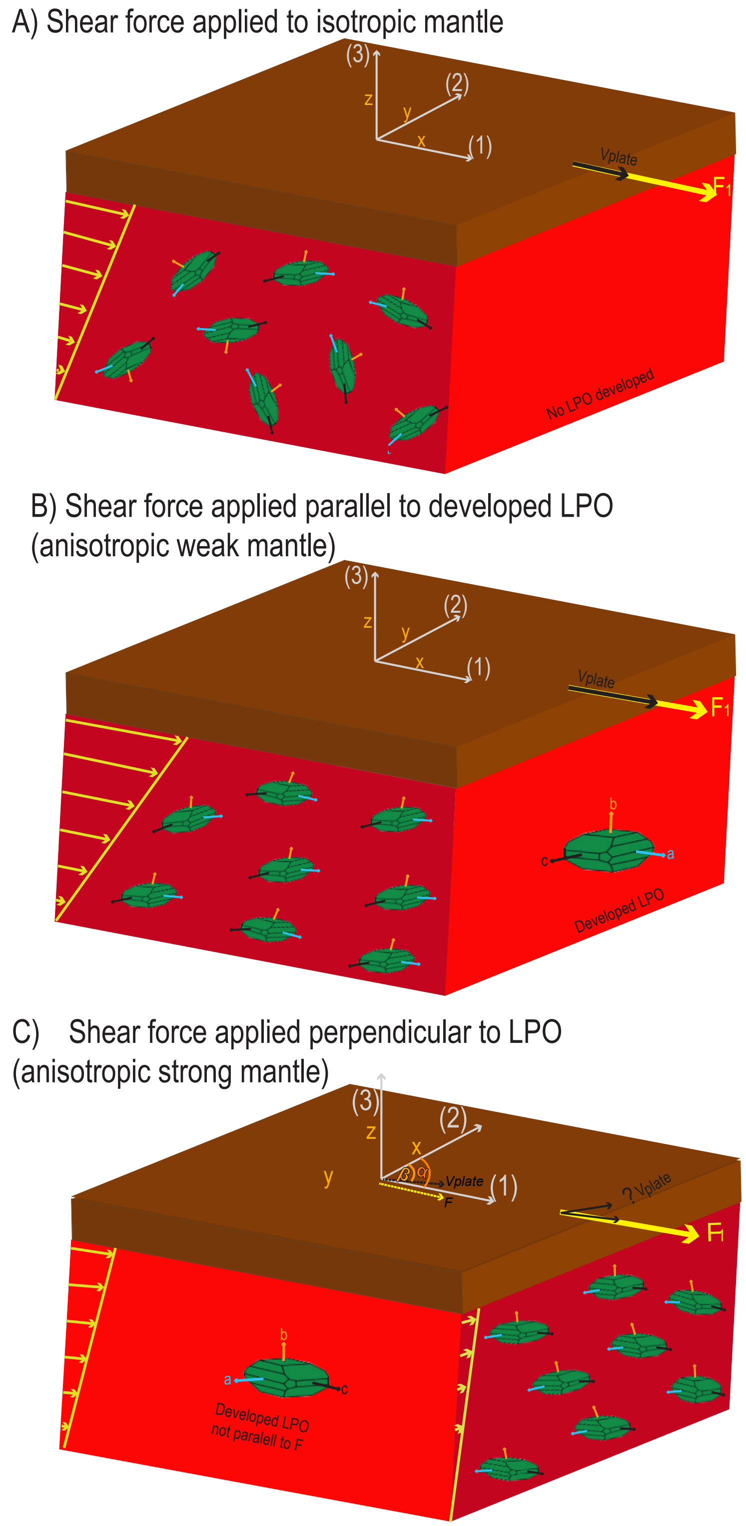

Figure 1: Relation between anisotropic viscosity and olivine texture formation. A) A force (F_1) applied to an initially isotropic asthenosphere (without a formed texture) yields a moderate plate speed. B) The same force applied parallel to the a-axis of a well-developed texture drives a much larger plate speed. C) Applying this force parallel to the c-axis causes the plate to move much more slowly. The configuration depicted in panel (B) can evolve into

the configuration depicted in panel (C) in two ways. Either the force can be rotated relative to the texture (as for many geodynamic scenarios) or the texture can be rotated with respect to the force (as illustrated in (C) and implemented in our modeling effort).

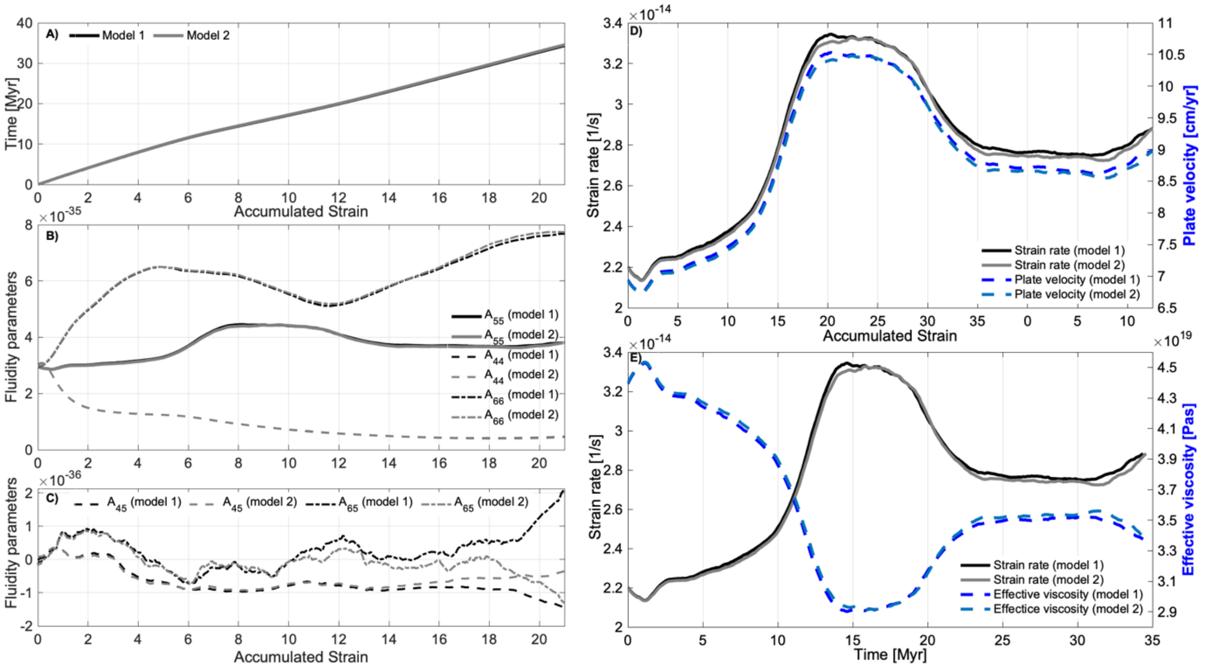

Figure 2: Results of two sets of models with constant shear stress (σ_{13} = 0.68 MPa), both computed as average results from 5 model runs each starting from 1000 uniformly distributed grain orientations. A) Accumulated strain as a function of time. B) Normal components of the fluidity parameter tensor. A_{44} and A_{66} are fictive curves since the associated stresses for these components, σ_{23} and σ_{12}, are zero. A_{55} represents the fluidity for the actual applied stress σ_{13}. C) Fluidity components relating strain rates in the perpendicular direction (A_{45}) or plane (A_{65}) with respect to the shear stress (σ_{13}). D) Strain rate and plate velocity as a function of the accumulated strain. The plate velocity is calculated from the horizontal strain rate component (normal to the (3) direction), while the strain-rate curve is the norm of the strain rate tensor (for which only the non-diagonal components are non-zero). E) Strain rate and effective viscosity as a function of time instead of accumulated strain.

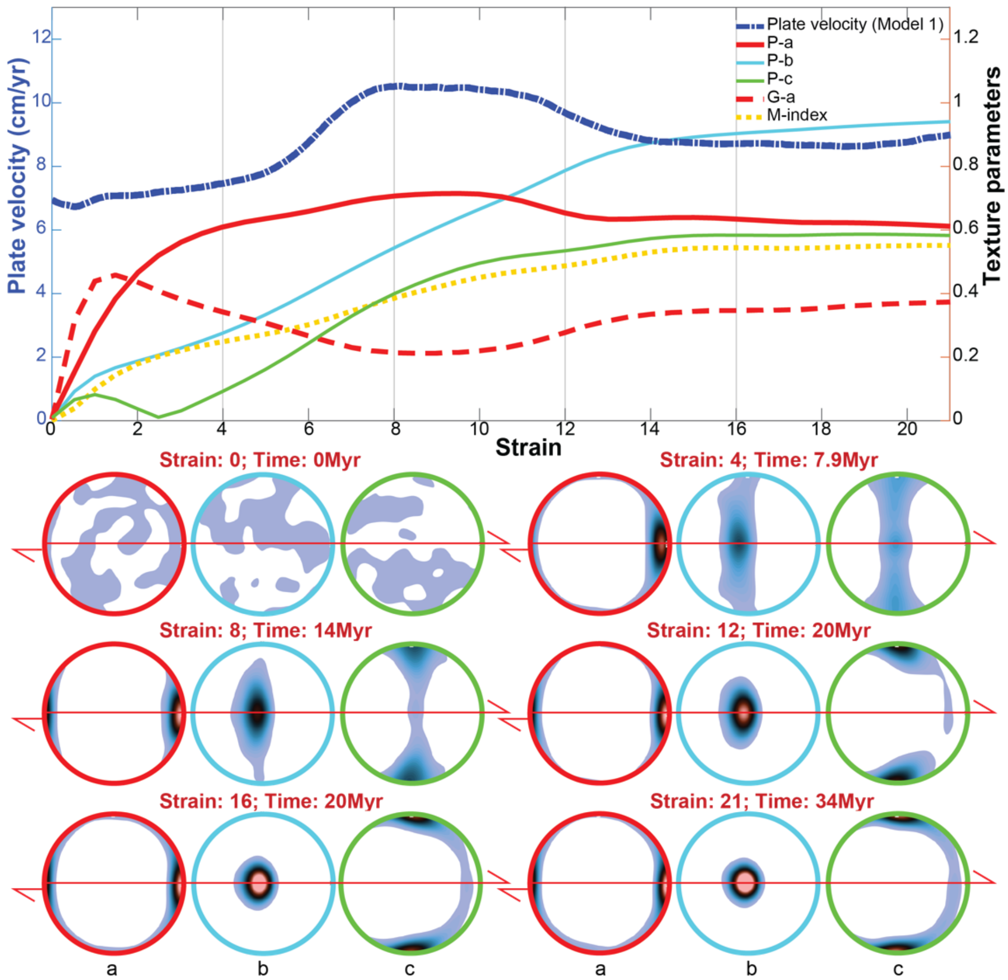

Figure 3: The evolution of plate velocity and several texture parameters as a function of accumulated strain (top panel) with pole figures (below) indicating the orientation density of a-, b-, and c- axes for olivine aggregates with different total strains. The shear direction (marked by red arrows) is towards the right and the shear plane is the same as the figure's plane.

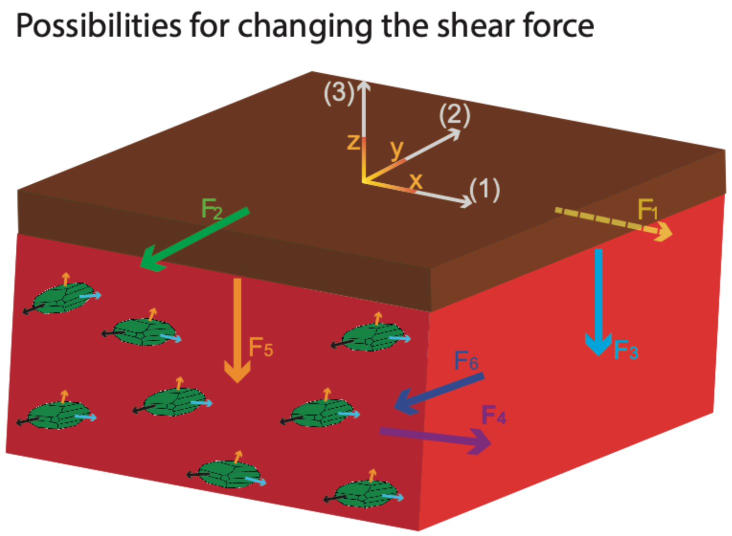

Figure 4: Possible orientations for the shear force, with F_1 representing the orientation associated with initial plate motion (e.g., as in Fig. 1b). F_2 represents a shear force acting on a horizonal plane at 90° to the initial plate motion direction, analogous to a change in the direction of the plate driving force. F_4 and F_6 represent forces that create shearing deformation in a horizontal direction along vertical planes, analogous to transform shear zones. F_3 and F_5 represent forces that create shearing deformation in a vertical direction on vertical planes, analogous to subduction initiation or a dripping instability. In our analysis, all forces have the same magnitude as F_1.

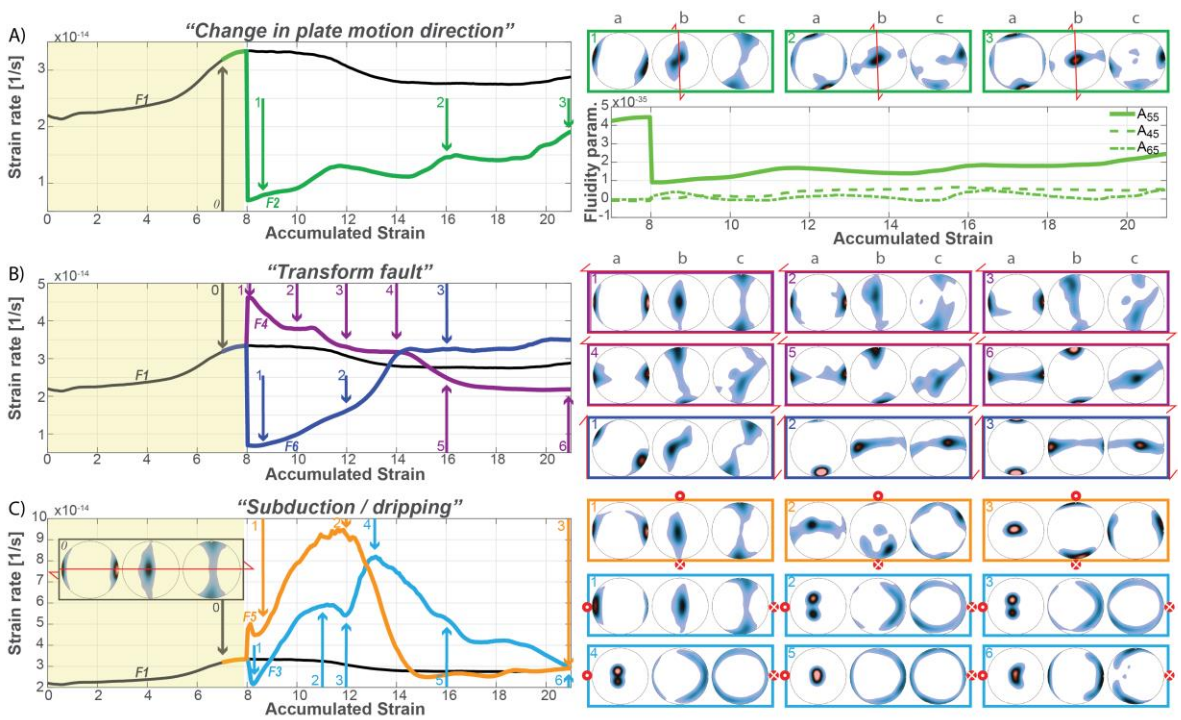

Figure 5: Strain rate as a function of accumulated strain for the five different changes to the imposed shear force (Fig. 4). On the left side, an initially isotropic aggregate is deformed

with shear force F_1 until a strain of 8 (as in Fig. 2D). At a strain of 8, the direction of the shear force is instantaneously changed to the directions F_2 through F_6 (Fig. 4). On the right side, pole figures indicate the texture for several points in the evolution denoted by arrows in the left diagrams. Note that all of the textures are presented relative to the mantle reference frame, and the shear force acting on the mantle is marked by red arrows (and arrow points and tails). In panel A) we present the fluidity components related to the actual shear stress for the case of a change in the direction of the plate driving force (F_1 changing to F_2).

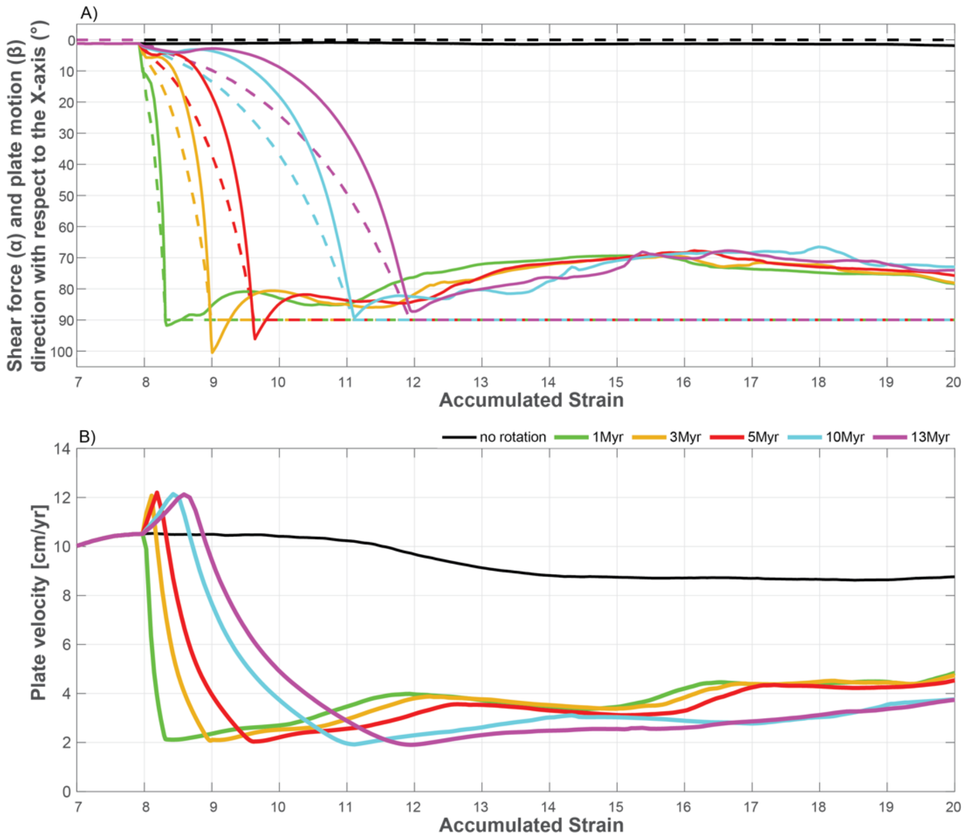

Figure 6: Results from models with different rates of imposed rotation of the shear stress. An initial texture (associated with an accumulated strain of 8, using model 1 of Fig. 2) is rotated 90° around the z-axis (representing a change from F_1 to F_2) within a period between 1 and 13 Myr. a) Change in the direction of the shear force (α, dashed lines) and plate motion (β, solid lines) with respect to the x-axis (fixed to the mantle), as a function of accumulated strain. b) Amplitude of the plate velocity as a function of accumulated strain.

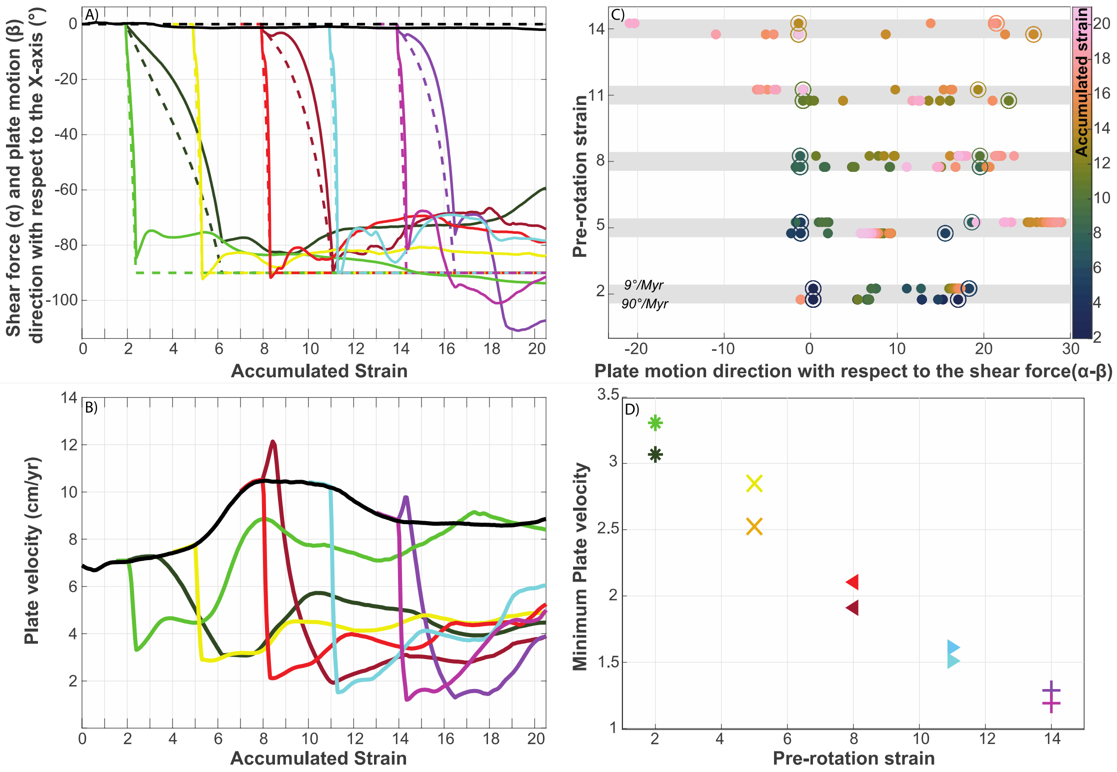

Figure 7: Results from models with varying amounts of accumulated strain (and therefore texture strength) at the time of the rotation (Pre-rotation strain). A) Direction of the shear force (α, dashed lines) and the plate motion (β, solid lines) for models that rotate the texture 90° in either 1 Myr (lighter colors) or 10 Myr (darker colors). B) Corresponding plate velocity amplitudes vs. accumulated strain for the cases shown in (A). C) Local minimums and maximums of the plate-motion direction marked with dots that are color-coded according the accumulated strain (with respect to the shear force direction) for the five tested switch strains. For each switch strain, upper rows represent models using the 10 Myr rotation time while the lower rows use 1 Myr rotations. D) Minimum plate velocity (i.e., velocity right after the rotation) vs. the accumulated strain after which the rotation has happened.

916
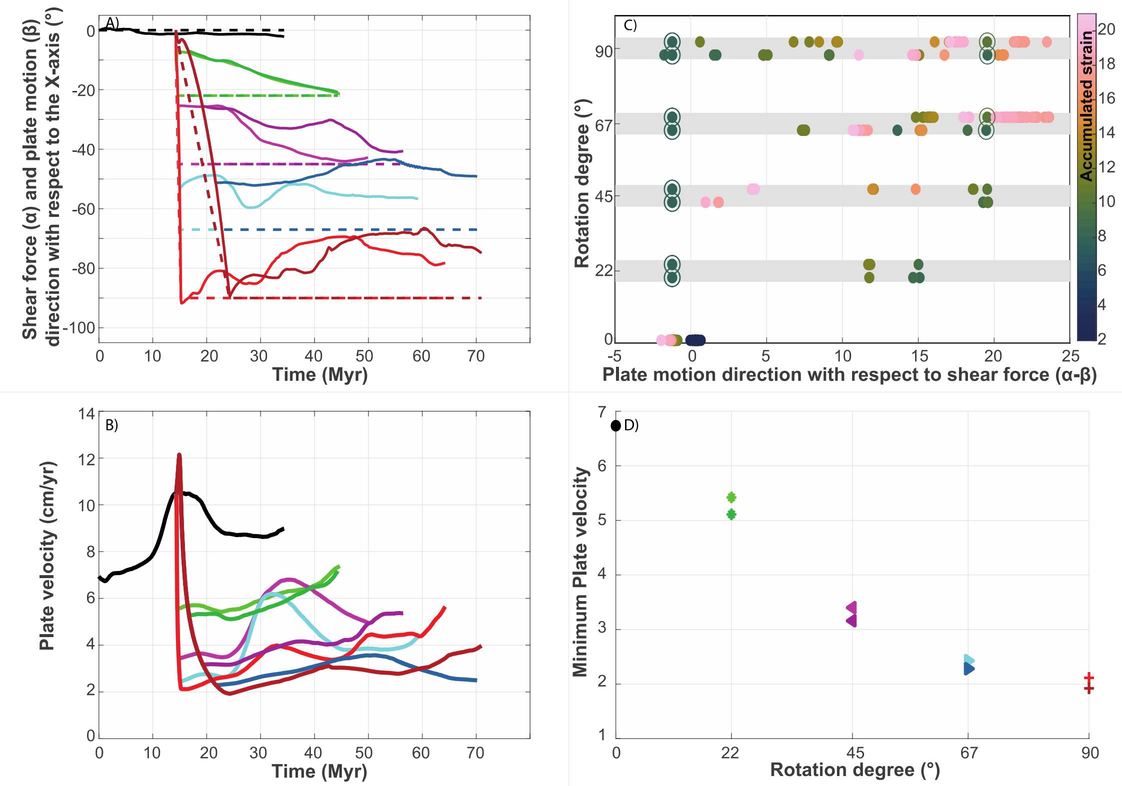

917 *Figure 8: Results from models with varying amounts of rotation around the z-axis. Panels are*
918 *the same as in Fig. 7, except using rotation angle instead of pre-rotation strain in (C) and*
919 *(D).*

920

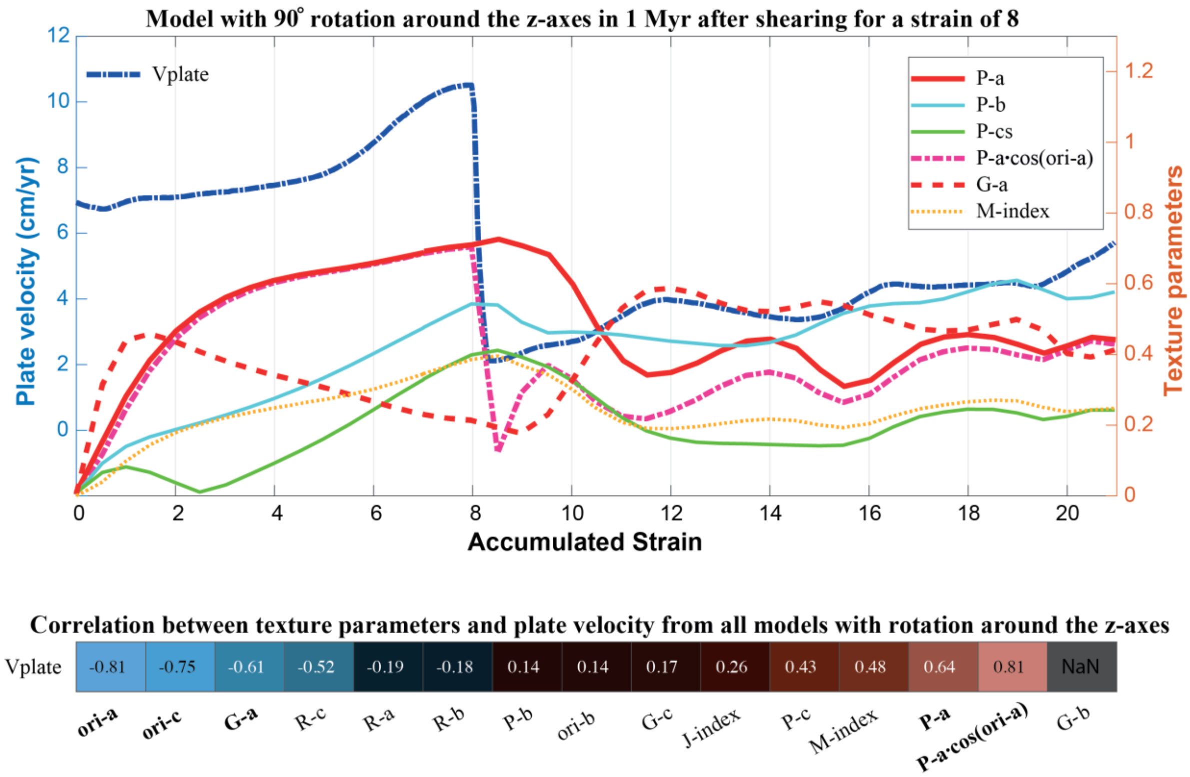

Figure 9: Top) plate velocity and texture parameters, as a function of accumulated strain, for a model in which 90° rotation (representing a change from F_1 to F_2) is imposed over 1 Myr after a strain of 8 (the fastest rotation presented in Fig. 6). Bottom) correlation between texture parameters and plate velocity based on all models with rotation (0-90°) around the z-axis, listed in order from negative (blue shades) to positive (red shades) correlations. Abbreviations: v_{plate} plate velocity; ori-a (-b; -c) mean orientation of the olivine a-axes (b-axes; c-axes); G, R, P (-a -b; -c) girdle, random, and point distribution parameters for each axes, respectively (Vollmer, 1990).

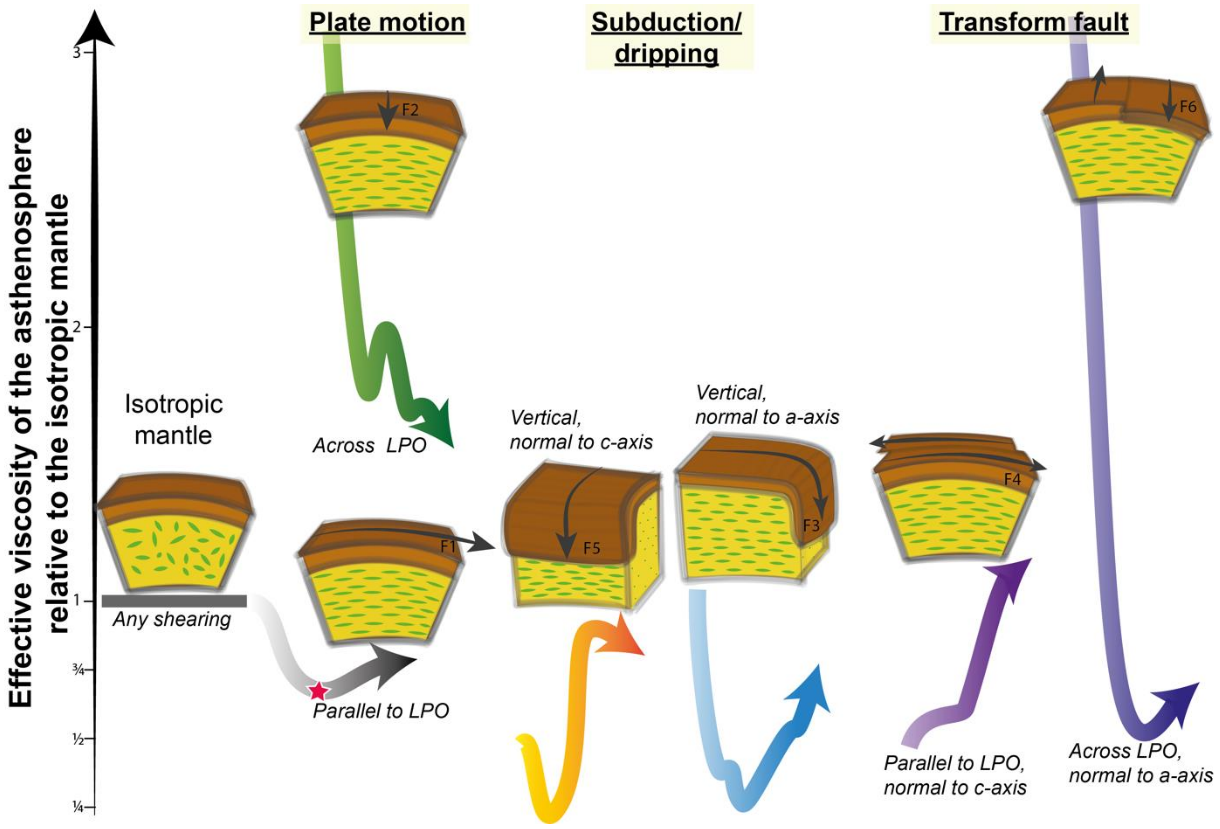

Figure 10: The effect of anisotropic viscosity in the asthenosphere, for different geodynamic situations. The white to black arrow indicates the mantle weakening path associated with development of an LPO as the asthenosphere accumulates strain due to simple shear (e.g. in model 1). The colored arrows indicate the time evolution of the effective viscosity from the moment of switching the shear direction (strain of 8, marked with a star on the white-to-black arrow) until a strain of 21 (based on results shown in Fig. 5). Geodynamic processes for which the effective viscosity elevates (F_2 plate motion and F_6 transform fault) will be initially impeded by anisotropic viscosity, while those for which the effective viscosity decreases (F_3 and F_5, subduction and dripping, and F_4 transform fault) will be initially promoted. Subsequent changes to the effective viscosity along each path indicate how continued texture development should either speed or slow each process as it develops.